Numerical investigations of the tulip flame instability -comparisons with experimental results

B. Nkonga* and G. Fernandez and H. Guillard and B. Larrouturou†

A two-dimensional adaptive finite-element code is used to numerically investigate the propagation of a laminar premixed flame in a closed rectangular chamber giving rise to the so-called tulip instability. The physical model includes a single one-step chemical reaction where the physical parameters involved in the model are chosen in order to adequately represent a stoichiometric methane-air flame. Attention is focused on the shape of the flame and the flowfield generated by the combustion process. A detailed comparison between the numerical results and available experimental data shows a very good agreement, for various sizes of the combustion chamber.

1. Introduction

The progress made in state-of-the-art numerical simulations of flame propagation phenomena in the last decade has been very important. This is not only due to the increase of the available computing power; to a larger extent, these improvements are related to the growing interest of an increasing number of researchers for the combustion science, and in particular for numerical combustion, which led to the development of several new algorithms especially designed and suited for flame calculations.

As an example of this evolution, we can simply mention that the test cases of the workshop on "Numerical methods in laminar flame propagation " (Peters and Warnatz, 1981) were concerning the unsteady propagation of a planar flame with one-step chemistry on one hand, and the steady hydrogen-air planar flame propagation on the other hand (and we should add that the high dispersion of the results obtained by the different participating groups clearly indicates that these test-cases, which now appear as basic problems of numerical combustion, were actually quite difficult at that time). In comparison, there exist now many multi-dimensional flame calculations whose results satisfactorily agree with experimental results; we can mention as an example two-dimensional calculations of steady flames with hydrocarbon chemistry (Smooke et al, 1988).

In this paper we present two-dimensional flame calculations and comparisons with experimental results. The problem under consideration concerns the unsteady propagation of a stoichiometric laminar methane-air flame in a closed rectangular vessel, and gives rise to the so-called "tulip flame instability" a - largely unexplained - physical phenomenon which has been of interest for several decades (see e.g. (Markstein,1964)). We use for comparisons the experimental results of Steinert et al. (1982), Dunn-Rankin (1985) and

*INRIA, Sophia-Antipolis, 06560 Valbonne, France.
†CERMICS,INRIA, Sophia-Antipolis, 06560 Valbonne, France.

Dunn-Rankin et al. (1986). As in Steinert et al. (1982), we also investigate the influence of the chamber length on the appearance and development of the tulip instability.

This problem has in fact been the subject of a few numerical investigations in the very last years: Cloutman (1988) and Hwang et al. (1987) have performed numerical investigations of this phenomenon in cylindrical ducts using the CONCHAS-SPRAY computer code; an inviscid, incompressible model has also been used by Dunn-Rankin et al. (1986); Fernandez and Guillard (1989.a) have presented some preliminary computations using the present numerical method, and Gonzalez et al. (to be published) have also recently numerically investigated the tulip flame phenomenon. One of the new features of the present work lies in the detailed comparisons with experimental results.

The calculation of an unsteady propagating methane-air flame which would include detailed chemical kinetics and transport models being extremely expensive, we had to use some simplifying hypotheses, and in particular to simplify the chemical mechanism: in the calculations reported here, we simply use a one-step chemical mechanism, the values of the different parameters involved in this model being chosen in order to provide the best possible representation of a methane-air flame. We will also assume that the reacting flow under consideration is inviscid. In fact, the viscous effects could be included without particular difficulty in our numerical method (see (Fezoui et al. 1989)), which would essentially affect the solution in the neighbourhood of the chamber walls. This assumption is based on our belief that the viscous effects play a secondary role in the investigated phenomenon (the same conclusion was reached by Dunn-Rankin et al (1986) ; for the Darrieus-Landau instability, the fact that the gas viscosity does not influence the instability at the leading order is well known; see Clavin (1985)). Thus, our analysis, where we a priori neglect the viscous effects, shows that the basic mechanisms which primarily govern the tulip instability are indeed not related to any viscous effect (such as a flame–boundary layer interaction).

Even with these simplifications, several great difficulties remain: in particular, the problem we are actually solving is extremely stiff: the ratio of the flame thickness over the chamber length is as small as 10^{-2} in the calculations with the longest vessel, and the Mach number in all computations reported below is as small as $2\ 10^{-3}$.

The plan of the paper is as follows. In Section 2, we briefly present the numerical methodology used in this study. The thermochemical model actually used in the calculations is described in detail in Section 3, and Section 4 is devoted to the presentation of the numerical results, together with the comparison with the experimental results of Steinert et al. (1982) and Dunn-Rankin (1985). Finally in Section 5, we give a brief discussion of the possible mechanisms responsible for the tulip flame formation.

2. Numerical Methodology

2.1. The general equations

We will concentrate on the simulation of multi-component inviscid laminar reacting gaseous flows. Our system of governing equations will therefore include the Euler equations, with additional continuity equations for each of the gaseous species, and with additional diffusive and reactive terms in the energy and in the species equations. We consider a gaseous mixture made of two species $\mathcal{R}$ and $\mathcal{P}$, where the one-step chemical

reaction $\mathcal{R} \longrightarrow \mathcal{P}$ is taking place, and we call Y the mass fraction of the reactant species $\mathcal{R}$. Using Fourier's and Fick's law to describe heat conduction and molecular diffusion, we write the *normalized* governing equations for this flow in conservative form as:

$$W_t + F(W)_x + G(W)_y = P(W, W_x)_x + Q(W, W_y)_y + S(W) \ , \tag{1}$$

with:

$$\left\{ \begin{array}{c} W = \begin{pmatrix} \rho \\ \rho u \\ \rho v \\ E \\ \rho Y \end{pmatrix} \ , \quad F(W) = \begin{pmatrix} \rho u \\ \rho u^2 + p \\ \rho uv \\ u(E+p) \\ \rho uY \end{pmatrix} \ , \quad G(W) = \begin{pmatrix} \rho v \\ \rho uv \\ \rho v^2 + p \\ v(E+p) \\ \rho vY \end{pmatrix} \ , \\ \\ P(W, W_x) = \begin{pmatrix} 0 \\ 0 \\ 0 \\ D_T T_x \\ D_Y Y_x \end{pmatrix} \ , \quad Q(W, W_y) = \begin{pmatrix} 0 \\ 0 \\ 0 \\ D_T T_y \\ D_Y Y_y \end{pmatrix} \ , \\ \\ S(W) = \begin{pmatrix} 0 \\ 0 \\ 0 \\ \mathcal{Q}\Omega \\ -\Omega \end{pmatrix} \ . \end{array} \right. \tag{2}$$

Our notations are classical : u and v are the components of the mixture velocity $\overrightarrow{U}$, p is the pressure, E is the sum of the internal and kinetic energies per unit volume, D_T is the normalized thermal conductivity, T the temperature, D_Y is the normalized molecular diffusion coefficient of species $\mathcal{R}$ and $\mathcal{P}$. The source term Ω is the reaction rate (a reaction term appears in the energy equation since E is not the total energy).

We assume that both species behave as perfect gases, and have the same specific heats C_v and C_p and the same molecular weight m^*; moreover, the reaction term is given by Arrhenius' law. System (1)-(2) is then completed by the following relations:

$$p = \frac{\rho T}{\gamma Ma^2} = (\gamma - 1)\left(E - \frac{1}{2}\rho(u^2 + v^2)\right) \ , \tag{3}$$

$$\Omega = Ar \rho Y \exp\left(-\frac{\mathcal{E}}{T}\right) \ , \tag{4}$$

$$D_T = \frac{1}{(\gamma - 1) Ma^2 PR} \ , \quad D_Y = \frac{1}{LePR} \ . \tag{5}$$

In these relations, the non-dimensional parameters Ar, γ, Le, Ma, $\mathcal{E}$ and $\mathcal{Q}$ are the normalized Arrhenius prefactor, the specific heat ratio, the Lewis number, a reference Mach

number, the normalized activation energy and the normalized heat release defined as follows:

$$Ar = t_0 \mathcal{A} \ , \quad \gamma = \frac{C_p}{C_v} \ , \quad Le = \frac{\lambda}{\rho_0 C_p D} \ , \tag{6}$$

$$Ma = \frac{u_0}{\sqrt{(\gamma - 1) C_p T_0}} \ , \quad \mathcal{E} = \frac{E_0}{\mathcal{R} T_0} \ , \quad \mathcal{Q} = \frac{Q Y_0}{m^* u_0^2} \ , \tag{7}$$

where l_0, u_0, $t_0 = l_0/u_0$, ρ_0, Y_0 and T_0 are the length, velocity, time, density, mass fraction and temperature units respectively; moreover, E_0 is the activation energy, $\mathcal{R}$ is the perfect gas constant, Q is the heat release, $\mathcal{A}$ is the dimensional Arrhenius prefactor, λ and D are the thermal and molecular diffusivity. The parameter PR has the expression:

$$PR = \frac{l_0 u_0 \rho_0 C_p}{\lambda} \ , \tag{8}$$

(for a viscous gas, PR would be the product of the Prandtl number and of the Reynolds number). We refer to Habbal et al. (1987) for the details about the normalization of system (1).

2.2. Spatial approximation

For the numerical solution of the above system of conservation laws, we will use the method employed in Fernandez and Guillard (1989.a,1989.b). The numerical scheme is an upwind mixed finite element – finite volume scheme, operating on unstructured finite-element triangulations; it is based on a series of works aimed towards the numerical solution of the Euler equations and of the reacting flow equations on unstructured meshes (see Fezoui (1985), Dervieux (1987), Benkhaldoun et al. (1988), Fernandez and Guillard (1989.a, 1989.b, 1989.c)). The ability of the scheme to operate on highly deformed meshes is an important feature of the method, which will allow us to use an adaptive grid for the thin flame calculations below.

We first present the scheme used for the spatial approximation of the above system; we will then examine in a second step the temporal integration scheme. In other words, we assume temporarily that a fully explicit integration scheme is used to advance in time the numerical solution.

Thus, we consider a finite-element triangulation of the computational domain. In order to derive a finite-volume formulation, we consider a dual partition of the domain in control volumes or cells : a cell C_i is constructed around each vertex S_i by means of the medians of the neighbouring triangles, as shown on Figure 1.

Figure 1. Cell $\mathcal{C}_i$

Integrating system (1) in the control volume C_i, we get:

$$\iint_{C_i} W_t dx + \int_{\partial C_i} (F\nu_i^x + G\nu_i^y) dl = \int_{\partial C_i} (P\nu_i^x + Q\nu_i^y) dl + \iint_{C_i} S(W) dx \ , \tag{9}$$

where $\overrightarrow{\nu_i} = (\nu_i^x, \nu_i^y)$ is the outward unit normal on ∂C_i. To approximate the convective fluxes, i.e. the second integral in (9), we use the now well-known fact that the system of the so-called multi-component Euler equations:

$$W_t + F(W)_x + G(W)_y = 0 \ , \tag{10}$$

with the pressure p given by (3), is a nonlinear hyperbolic system of conservation laws (see e.g. Abgrall (1988), Fernandez and Larrouturou (1989)). This allows one to extend to gaseous mixtures most of the upwind schemes designed for the single-component equations (see Larrouturou and Fezoui (1989)). We use here an extension to mixtures of Roe's scheme (Roe, 1981). Given two states W_L and W_R and a vector $\overrightarrow{\eta} = (\eta^x, \eta^y)$, we define a numerical flux function Φ by:

$$\Phi(W_L, W_R, \overrightarrow{\eta}) = \frac{1}{2}[\mathcal{F}_\eta(W_L) + \mathcal{F}_\eta(W_R)] + \frac{1}{2}|\tilde{H}_\eta|(W_L - W_R) \ . \tag{11}$$

In this expression, we have set $\mathcal{F}_\eta(W) = \eta^x F(W) + \eta^y G(W)$, and $\tilde{H}_\eta = \tilde{H}_\eta(W_L, W_R)$ is a diagonalisable matrix satisfying Roe's property:

$$\mathcal{F}_\eta(W_L) - \mathcal{F}_\eta(W_R) = \tilde{H}_\eta(W_L, W_R)(W_L - W_R) \ ; \tag{12}$$

the matrix $|\tilde{H}_\eta|$ is defined using the diagonalization of $\tilde{H}_\eta$: if $\tilde{H} = T\tilde{\Lambda}T^{-1}$ with $\tilde{\Lambda}$ diagonal, $\tilde{\Lambda} = diag(\tilde{\lambda}_k)_{k=1,5}$, then we set $|\tilde{H}| = T|\tilde{\Lambda}|T^{-1}$, with $|\tilde{\Lambda}| = diag(|\tilde{\lambda}_k|)_{k=1,5}$.

Now, we write the second integral in (9) as:

$$\int_{\partial C_i} (F\nu_i^x + G\nu_i^y) = \sum_{j \in \mathcal{K}(i)} \int_{\partial C_{ij}} (F\nu_i^x + G\nu_i^y) \ , \tag{13}$$

where $\mathcal{K}(i)$ is the set of neighbouring nodes of S_i, and where $\partial C_{ij} = \partial C_i \cap \partial C_j$. Then, defining the vector $\overrightarrow{\nu_{ij}} = (\nu_{ij}^x, \nu_{ij}^y)$ by:

$$\nu_{ij}^x = \int_{\partial C_{ij}} \nu_i^x \ , \quad \nu_{ij}^y = \int_{\partial C_{ij}} \nu_i^y \ , \tag{14}$$

we obtain a first-order accurate upwind approximation of the convective flux (13) by:

$$\int_{\partial C_i} (F\nu_i^x + G\nu_i^y) = \sum_{j \in \mathcal{K}(i)} \Phi(W_i, W_j, \overrightarrow{\nu_{ij}}) \ . \tag{15}$$

A second-order accurate upwind extension can be derived by using a MUSCL-type approximation instead of a constant-by-cell approximation (see van Leer, 1974). In this case, (15) becomes:

$$\int_{\partial C_i} (F\nu_i^x + G\nu_i^y) = \sum_{j \in \mathcal{K}(i)} \Phi(W_{ij}, W_{ji}, \overrightarrow{\nu_{ij}}) \ , \tag{16}$$

where the numerical flux function Φ of (11) is again used, but where W_{ij} (resp.: W_{ji}) is a second-order accurate approximation of W at the cell interface ∂C_{ij} inside the cell C_i (resp.: inside the cell C_j). The construction of these states W_{ij} and W_{ji} involves the evaluation of "limited slopes" for each variable in each cell, in order to provide non-oscillatory results. We refer to Fezoui (1985) and Fezoui and Dervieux (1989) for the details.

Then, we consider the diffusive term $\int_{\partial C_i}(P\nu_i^x + Q\nu_i^y)$ in (9), which only involves the integrals $\int_{\partial C_i} \overrightarrow{\nabla} T.\overrightarrow{\nu_i}$ and $\int_{\partial C_i} \overrightarrow{\nabla} Y.\overrightarrow{\nu_i}$. To evaluate these terms, we consider here that the integrands are constant in each triangle τ of the triangulation. More precisely, we consider that, in a triangle τ with vertices S_j $(1 \leq j \leq 3)$, we have:

$$\nabla T|_\tau = \sum_{j=1}^{3} T_j \nabla \phi_j \ , \tag{17}$$

where ϕ_j is the P1 finite-element basis function associated to vertex S_j. Then the diffusive term in (9) takes the value:

$$\int_{\partial C_i}(P\nu_i^x + Q\nu_i^y) = \sum_{\tau \in \mathcal{T}(i)} \overrightarrow{\begin{pmatrix} P_\tau \\ Q_\tau \end{pmatrix}}.\int_{\partial C_i \cap \tau} \overrightarrow{\nu_i} \ , \tag{18}$$

where P_τ, Q_τ are the constant values of P and Q in the triangle τ. It is easy to check that (17)-(18) is equivalent to a classical finite-element discretization of the diffusive terms.

Lastly, we simply evaluate the reactive term in (9) as:

$$\int\int_{C_i} S(W) = S(W_i)\ area(C_i) \ . \tag{19}$$

2.2.1. Time integration

In order to motivate our choice for the time integration scheme used below, let us first examine the different characteristic time scales involved in the discrete problem. Calling Δh, c and U typical values of the mesh size, the sound speed and the mixture velocity (or the flame speed) respectively, we can identify four different time scales. The convective and acoustic time scales are defined as:

$$\Delta t^c = \frac{\Delta h}{U} \ , \quad \Delta t^a = \frac{\Delta h}{c} \ , \tag{20}$$

the diffusive time scale is:

$$\Delta t^d = \frac{\Delta h^2}{2D} \ , \tag{21}$$

and we also have to consider a reactive time scale Δt^r, equal to the characteristic time of the chemical reaction at the highest temperature in the mixture.

Of course, if a fully explicit time integration scheme is used, the time step Δt cannot exceed any of these time scales:

$$\Delta t \leq \min(\Delta t^a, \Delta t^c, \Delta t^d, \Delta t^r) \ . \tag{22}$$

In fact, what we wish to do for an accurate transient description of the flame propagation is to use in the calculations a time step of the order of magnitude of Δt^c or Δt^r. But a simple dimensional analysis shows that $\dfrac{\Delta t^d}{\Delta t^c} \approx \dfrac{\Delta h}{2L_f}$, where L_f is the flame thickness (we have simply used the fact that the product of the flame thickness by the flame velocity is close to the diffusion coefficient D). Therefore, in an accurate calculation, where several grid points are clustered in the thin reaction zone inside the flame thickness, the ratio $\dfrac{\Delta t^d}{\Delta t^c}$ is small. Besides this, the ratio $\dfrac{\Delta t^a}{\Delta t^c}$ is even smaller (this ratio is obviously equal to the Mach number). This shows that efficiency dictates to integrate both acoustic and diffusive terms implicitly, while treating the reactive term explicitly. In fact, we will integrate all fluxes F, G, P and Q implicitly.

The implicit integration of the diffusive term uses a classical linearized implicit formulation (see (Fernandez and Guillard, 1989.a) for more details). For the convective and acoustic numerical fluxes, whose expression (11) is not differentiable, we use an approximate linearization. Using the homogeneity property of the physical fluxes F and G, we rewrite (11) as:

$$\begin{aligned} \Phi(W_L, W_R, \overrightarrow{\eta}) &= \tfrac{1}{2}\left(\tfrac{\partial \mathcal{F}_\eta}{\partial W}(W_L)W_L + \tfrac{\partial \mathcal{F}_\eta}{\partial W}(W_R)W_R\right) + \tfrac{1}{2}|\tilde{H}_\eta|(W_L - W_R) \\ &= \tfrac{1}{2}\left(\tfrac{\partial \mathcal{F}_\eta}{\partial W}(W_L) + |\tilde{H}_\eta|\right) W_L + \tfrac{1}{2}\left(\tfrac{\partial \mathcal{F}_\eta}{\partial W}(W_R) - |\tilde{H}_\eta|\right) W_R \ . \end{aligned} \tag{23}$$

Writing this expression as $\mathcal{A}_{\overrightarrow{\eta}} W_L + \mathcal{B}_{\overrightarrow{\eta}} W_R$, we set, in view of (15):

$$\int_{\partial C_i} (F\nu_i^x + G\nu_i^y) = \sum_{j \in \mathcal{K}(i)} \Phi_{ij}^{n+1} \ , \tag{24}$$

where the implicit fluxes Φ_{ij}^{n+1} have the following expression:

$$\Phi_{ij}^{n+1} = \Phi(W_{ij}^n, W_{ji}^n, \overrightarrow{\nu_{ij}}) + \mathcal{A}_{\overrightarrow{\nu_{ij}}}(W_i^{n+1} - W_i^n) + \mathcal{B}_{\overrightarrow{\nu_{ij}}}(W_j^{n+1} - W_j^n) \ . \tag{25}$$

Notice that we use the limited second-order approximation for the explicit part of Φ^{n+1}.

The overall scheme is written as a linear system in δ-form (that is, we solve at each time step for the difference $W^{n+1} - W^n$ instead of solving directly for W^{n+1}), whose solutions is obtained using an unfactored symmetric Gauss-Seidel iteration. The resulting scheme is first-order accurate in time. In the computations presented below, the time step has been limited by the chemical time step Δt_r and corresponds to a CFL number between 50 and 150.

2.2.2. Boundary conditions

Let us end with some indications on the numerical boundary conditions used in the computer code. Call Γ the boundary of the computational domain and $\overrightarrow{n}$ the outward unit normal on Γ. The whole boundary Γ is supposed here to represent a solid wall.

In our scheme, we do not treat a boundary condition by forcing the value of a variable to a prescribed boundary value, but consider instead the integral formulation (4) and apply the boundary conditions by modifying the flux integrals on ∂C_i for those cells C_i

such that $\partial C_i \cap \Gamma \neq \emptyset$. In other words, for a vertex S_i located on Γ, we do not impose the slip condition $\overrightarrow{U}.\overrightarrow{n} = 0$, but take this condition into account in the evaluation of the convective fluxes, getting:

$$\int_{\partial C_i \cap \Gamma} Fn^x + Gn^y = \begin{pmatrix} 0 \\ \int_{\partial C_i \cap \Gamma} pn^x \\ \int_{\partial C_i \cap \Gamma} pn^y \\ 0 \\ 0 \end{pmatrix} \; ; \tag{26}$$

here, the pressure integrals are computed as:

$$\int_{\partial C_i \cap \Gamma} pn^x = p_i \int_{\partial C_i \cap \Gamma} n^x \; , \quad \int_{\partial C_i \cap \Gamma} pn^y = p_i \int_{\partial C_i \cap \Gamma} n^y \; . \tag{27}$$

Moreover, assuming that the wall is adiabatic and non catalytic ($\overrightarrow{\nabla} T.\overrightarrow{n} = 0$ and $\overrightarrow{\nabla} Y.\overrightarrow{n} = 0$ on Γ), we set:

$$\int_{\partial C_i \cap \Gamma} Pn^x + Qn^y = 0 \; . \tag{28}$$

2.2.3. Adaptive mesh strategy

We use the simple adaptive mesh algorithm of Benkhaldoun and Larrouturou (1987) in our calculations. The two-dimensional mesh is divided into straight lines parallel to the tube walls (in the direction where the flame propagates), and has the structure $N_{i,j} = [x(i,j), y(j)]$ (see Figure 6). When we wish to adapt the grid, we apply the one-dimensional equidistributing procedure described below to each line $y = y(j_0)$: this has the effect of concentrating many of the nodes N_{i,j_0} in the region where the curved flame front crosses the line $y = y(j_0)$. We then simply obtain the new triangulation by dividing each quadrangle $[N_{i,j},\ N_{i+1,j},\ N_{i+1,j+1},\ N_{i,j+1}]$ into two triangles $[N_{i,j},\ N_{i+1,j},\ N_{i+1,j+1}]$ and $[N_{i,j},\ N_{i+1,j+1},\ N_{i,j+1}]$.

The one-dimensional procedure employed for each line $y = y(j_0)$ works as follows: at some time levels during the calculation the "old" grid ($x^{old}(i,j_0)$) is changed to a new better grid ($x^{new}(i,j_0)$). To determine the new nodes locations, we evaluate a "mesh function" w, which indicates where a fine mesh is needed, and the new mesh is found by equidistributing w. Once the new mesh is known, the variables are interpolated from the old grid to the new one; for each line $y = y(j_0)$, this is again a one-dimensional procedure. We refer to Benkhaldoun and Larrouturou (1987) for more details.

Of course, this very simple adaptive procedure is designed for problems where the flame front actually crosses all mesh lines $y = y(j_0)$; it can indeed be seen on Figure 6 that this procedure provides a nicely adapted mesh, in particular with a good resolution of the reaction zone, when the flame has reached the horizontal tube walls. In the former stage of the phenomenon, that is before the flame reaches the tube walls, we do not use the above procedure and simply employ a fixed mesh (which is nevertheless finer in the left part of the chamber).

3. The Physical model

In the derivation of the physico-chemical model, simplifying assumptions are made. Although, in many respect the model may seem over-simplified, we believe that it retains the essential features of those combustion phenomena which are relevant to the tulip formation.

First of all, we suppose that the flow is inviscid, we neglect the external forces, and assume that the quantities λ, ρD, C_v and C_p and thus the non-dimensional numbers appearing in (1)-(8) are constant.

Then, in order to compare our results with the experimental data of Steinert et al. (1982), we have to adjust the parameters governing this simplified model to fit the characteristics of the methane-air flame. We first determine the molecular weight m^* of our equivalent species $\mathcal{R}$ and $\mathcal{P}$ by considering the overall reaction describing methane-air combustion:

$$CH_4 + 2O_2 + 2\frac{1-\alpha}{\alpha}N_2 \longrightarrow CO_2 + 2H_2O + 2\frac{1-\alpha}{\alpha}N_2 \tag{29}$$

where α is the proportion of nitrogen in air and take as value of m^*:

$$m^* = m_{CH_4} + 2m_{O_2} + 2\frac{1-\alpha}{\alpha}m_{N_2} \ , \tag{30}$$

where m_k is the molecular weight of specie k.

In the experiments of Steinert et al. (1982), the pressure and temperature of the fresh gases are:

$$P_u = 1 \ atm = 1.12 \ 10^5 \ Pa \ , \quad T_u = 298^o K \ . \tag{31}$$

The fresh gases temperature is used as the temperature unit: $T_0 = T_u$. Let $\mathcal{R}$ be the perfect gas constant, thus the density of the fresh gases is given by:

$$\rho_u = \frac{P_u m^*}{\mathcal{R} T_u} \simeq 1.15 kg/m^3 \ . \tag{32}$$

The non-dimensionalisation of the equation uses this value of the density as reference density : $\rho_0 = \rho_u$. The other parameters governing this simplified chemical mechanism are the activation energy E_0, the Arrhenius prefactor $\mathcal{A}$, the Lewis number Le, the parameter PR and the heat of reaction Q. In order to avoid any possible development of thermo-diffusive instabilities, we have simply chosen a Lewis number equal to unity. The heat of reaction is evaluated by considering a constant pressure combustion with the same burnt gas temperature as the methane-air combustion. Using the results of Tsatsaronis (1978), the burnt gas temperature corresponding to a fresh gas temperature of $T_u = 298^o K$ is taken equal to $T_b = 2200^o K$. This gives the following value of the heat of reaction:

$$Q = \frac{m^* C_p (T_b - T_u)}{Y_u} \ . \tag{33}$$

where $Y_u = Y_0 = 1.$ and where the specific heat at constant pressure C_p is defined by $C_p = \dfrac{\gamma \mathcal{R}}{(\gamma - 1) m^*}$ with $\gamma = 1.4$.

Estimating the activation energy is difficult. However as the ratio of the reaction zone thickness over the flame thickness scales with the Zeldovich number $\beta = \frac{E_0(T_b - T_u)}{\mathcal{R}T_b^2}$, it is advantageous from a computational viewpoint to use a rather low value of the activation energy. Here we take:

$$\beta = 4.323 \ . \tag{34}$$

It remains to define the Arrhenius prefactor Ar and the parameter PR. To do that, we consider the flame speed and the flame thickness of a methane-air flame. Considerable dispersion of the evaluation of the value of these parameters still exists in the literature: the reported flame speeds vary from 33 cm/s to 46 cm/s, while the flame thickness ranges from 0.5 mm to 1.5 mm. We choose here an average value of $V_{flame} = 40\ cm/s$ for the flame velocity and (for computational reasons) the largest flame thickness:$L_{flame} = 1.5\ mm$. These values are taken as reference values in the non-dimensional equations, $l_0 = L_{flame}$ and $u_0 = V_{flame}$.

With these choices and using the results of the asymptotic analysis for high activation energy, we obtain (Bush, Fendel, 1970) :

$$PR = 1 \ , \quad Ar = \frac{\beta^2}{2Le}\frac{T_u}{T_b} exp(\frac{\mathcal{E}}{T_b/T_0}) = 1.023.\ 10^4 \ . \tag{35}$$

However, these results are only valid in the limit $\beta \to \infty$. In order to fit more closely the experimental results, we have to adjust these values such that the computed flame speed and flame thickness agree with the experimental ones. We have then performed a serie of one-dimensional computations in order to optimize these coefficients. This results in the following new values of these parameters: $Ar = 1.33\ 10^4$ and $PR = 1$. The computed flame speed using these optimized values is $V_{flame} = 40.30\ cm/s$, which can be considered as satisfactory.

4. Numerical results and comparison with experiments

The propagation of a flame in a closed tube can be divided into three general phases (described as cylindrical, planar and folded by Steinert et al. (1982)). We describe here these different phases in the case of a rectangular box of dimension $L_x = 155\ mm$ x $L_y = 38.1\ mm$ (the longest tube considered in the experiments of Steinert et al. (1982)) with reference to Figure 6 that displays the evolution of the reaction rate contours and to Figure 2 that shows the pressure history.

In the initial phase of propagation, the flame develops a semi-circular shape centered at the ignition point. It first expands uniformly while keeping its semi-circular shape until it approaches the side walls, then it takes an elongated elliptical form with sections almost parallel to the side walls. During this first period, the surface area of the flame is continuously increasing. This phase corresponds in the pressure plot to the rapid rise of the pressure from $t = 0$ to $t \simeq 12\ ms$ and ends with the steep change of dP/dt at $t \simeq 12\ ms$ that can be seen in the pressure plots. Some authors (Leyer and Manson, 1971), (Starke and Roth, 1986) have reported the appearance of periodic pressure vibrations at the end of this first phase. These pressure fluctuations are absent in the present calculations as in

the experiments of Steinert et al. (1982). In the next phase extending to $t \simeq 28\ ms$ the pressure increases almost linearly. Confrontation with the reaction rate contours shows that this phase corresponds to the vanishing of the upper and lower part of the flame by wall quenching. The surface area of the flame decreases while the flame flattens. The end of this period sees the very rapid formation of the tulip flame which occurs between $t \simeq 24\ ms$ and $t \simeq 28\ ms$. The last stage of the combustion process is concerned with the developpement of the tulip flame. The central part of the flame propagates more slowly than the upper and lower part resulting in the developpement of a stable inverted conical flame shape. The flame surface area increases again in this last period resulting in a more rapid rise of the pressure than in the previous phase.

The agreement with the experimental data of Steinert et al. (1982) is good. The comparison between the experimental and numerical results (Figure 6 and 2) shows that the three different phases occur approximately at the same time (approximately $12-13\ ms$ for the end of the cylindrical phase and between 24 ms and 28 ms for that of the planar phase). The location of the tulip formation is also approximatively the same : $80\ mm \leq x \leq 90\ mm$ in the experiments and $75\ mm \leq x \leq 85\ mm$ for the numerical results. There are some discrespancies in the pressure values: the computed pressures differ from the measured ones by some tens of kPa. This is due to the adiabatic boundary conditions used in the computations that give larger value of the pressure than in the experiments where the walls are non-adiabatic.

The occurence of the tulip flame is highly dependent of the aspect ratio of the tube and for $L_x/L_y < 2$ no tulip formation is observed. This feature has been noticed by many investigators and for instance the numerical calculations of flame propagation in a short closed vessel reported in Fernandez and Guillard (1989.b,1989.c) show no development of tulip instabilities. Here, we have computed the propagation of a flame in a 30 mm long tube (with the tube width unchanged), which is the shortest considered in the experiments of Steinert et al. (1982). Figure 6 shows the reaction rate contours in this case compared with the experimental results of Steinert et al. (1982). As in the experiments, no tulip formation can be seen and the central part of the flame remains concave in the direction of the burned gases.

We have also reproduced the experiment of Steinert et al. (1982) with a 120 mm long tube (aspect ratio $L_x/L_y \simeq 3.15$). The tulip formation can be seen to occur at $x \simeq 65\ mm$ (Figure 6). However, the shape of the flame front is rather different from the 150 mm case. Instead of a slowing down of the central part of the flame, the tulip is formed because the slower portions of the flame are now located between the wall and the symmetry axis. This results is the formation of a double-lobe flame. It is interesting to note that the experimental data of Steinert et al. (1982) also shows this two-fold shape (compare Figure 6.a and 6.b).

We now turn to a description of the hydrodynamical field generated by the flame during its propagation and compare them with the velocity fields obtained with Laser Doppler Anemometry (LDA) for the 155 mm case considered by Dunn-Rankin (1985) and Dunn-Rankin and Sawyer (1985). Recent results using LDA have also been reported by Jeung et al. (1989) for a propane/air flame in a 150 mm x 50 mm x 50 mm tube.

In its first phase of propagation that extends approximately to $t \simeq 12\ ms$, before the flame reaches the walls, the flow at both sides of the flame is directed toward the

unburnt gases. Examination of Figure 3 showing an enlarged view of the velocity field at $t = 9.3\ ms$ reveals that the "side" portions of the flame generate a flow directed towards the centerline. This flow is canalized in the longitudinal direction due to the confining effects of the ignition and side walls. The acceleration due to these converging velocities is able to maintain a positive velocity everywhere in the tube although in the burnt gases the expansion due to the flame and the canalized flow are of opposite sign. On the contrary, in the unburnt gases, the expansion due to the flame adds to the canalized flow and this results in the generation of large velocities of the order of 10 m/s. These gross features of the flow are in agreement with the experimental results of Dunn-Rankin (1985) who also found maximun velocities of the order of 10 m/s, and are confirmed by the experimental and numerical results of Jeung et al. (1989) and Hwang et al. (to be published).

This phase of the flame propagation ends when the flame reaches the side walls. The next phase corresponds to a flattening of the flame and ends at approximately $t \simeq 28\ ms$ when some premises of the appearance of the tulip flame can be noticed. During this phase, important changes occur in the flow. First, it appears that the flame shape has a very localized influence on the velocity field and that, except in the vicinity of the flame, the flow is almost one-dimensional and is very similar with the flow generated by a planar flame. Second, the disappearance of the "side" portions of the flame resulting in a decrease of flame area produces a net reduction of the flow velocities : at $t \simeq 24\ ms$, when the flame is almost planar, the maximum velocity is only of the order of 4 m/s. Finally, this phase is also characterized by the appearance of negative velocities in the burnt gases. This event coincides with the time when the flame reaches the walls, as can be seen on Figure 4 which shows a blow-up of the velocity field near the flame front at $t = 13.02\ ms$. This is the main difference between the present numerical result and the experimental data, since the latter show the persistence of positive velocities in the burnt gases almost until the emergence of the tulip shape. We note on Figure 4 the presence of a divergence zone clearly separating a region of positive velocities from a region of negative velocities. Due to the adaptive mesh used in this computation, this zone is accurately described. Previous experimental and numerical works did not have such a nice representation due to the coarse LDA or numerical meshes used. While one can be tempted to identify the region on the left of this zone with burnt gases and the region on the right with unburnt, it must be emphasized that this is not the case: examination of the governing equations and of the numerical results shows that the divergence zone is localized in the preheat zone and thus that this zone contains a large amount of fresh gases. As it can be noticed that a net transport along the flame front (and thus a net transport of fresh gases) occurs in the divergence zone from the walls to the medium zone, this accurate representation of the structure of the flame (that is absent from flame sheet models or numerical computations using non-adapted meshes) may have its importance for the tulip formation.

Between $t \simeq 13$ and $t \simeq 24\ ms$, as the flame becomes more and more planar, the main feature of the flow is the development of a zone of recirculating flow near the side wall in the burnt gases. This is shown in Figure 5 that displays profiles of the horizontal velocity on the wall (the positive horizontal velocities at the wall correspond to the recirculation zone). It can be noticed that this rotational structure moves back through the burnt gases and does not follow the flame in its propagation. Such conclusions are also present in the experimental work by Dunn-Rankin (1985) as well as in Jeung et al. (1989) and Hwang

et al.(1987).

The tulip formation occurs between $t \simeq 24ms$ and $t \simeq 31.5$ ms. Figure 6, 6 and 6 show an enlarged view of the velocity fields near the flame zone. Note that the horizontal gas velocity is higher at the walls than on the mid-line in the fresh gases, whereas it is smaller (in absolute value) at the walls than on the mid-line in the burnt gases. The recirculation zone behind the flame again appears on the first plot.

Figure 6 shows the velocity field at $t = 44.65$ ms when the tulip flame is fully developped. The presence of a large stagnation region inside the cusp of the tulip flame is now well documented and has been also reported in the experimental data of Dunn-Rankin (1985). We also note the large difference between the value of the velocity inside the burnt gases and the small value in the unburnt gases. It is also interesting to note that the velocities are almost perpendicular to the flame front in the reaction zone region. Once the tulip has been formed, this shape appears to be very stable and no further modifications of the essential features of the flow can be seen until the end of the computations.

5. Discussion

The reasons of the formation of the tulip flame have been investigated by researchers for more than 60 years, and several hypotheses have been put forward to explain this phenomenon. The earliest explanation (Guénoche, 1964) has attributed the tulip flame phenomenon to pressure waves interactions with the flame. In the low Mach number context of the present investigation, the experiments and the numerical results have shown that no significant pressure waves are present and this explanation can be ruled out. Other possible explanations of tulip flame formation have advocated purely fluid dynamics causes: the existence of a vortex created in the burnt gases near the side walls has been proposed as a possible explanation in Dunn-Rankin and Sawyer (1985). However, in view of the present results where the vortex appears long before the tulip formation and is left behind the flame front as this one moves toward the unburnt gases, this does not seem to have a definite link with the development of the instability. Moreover, it is worth mentioning that this explanation has been abandoned by the previous authors when the numerical work by Dunn-Rankin et al. (1986), who use an incompressible inviscid model, revealed that vorticity is not necessary to create a tulip flame.

A different (but related) fluid mechanical cause is put forward in Jeung et al. (1989), Hwang et al. (to be published) and Gonzalez et al (to be published). These authors observe the formation of what they call "squish" flow near the side walls. This flow is due to the compression and acceleration of the unburnt gases trapped between the side walls and the flame front. The present results do not support this explanation; no evidence of a significant acceleration of the unburnt gases when the flame reaches the side walls (see Figure 6) can be noticed. In a similar way, it appears from our experiments that the development of the tulip flame instability is not related to a flame-boundary layer interaction.

Finally, the last kind of explanations resorts to the development of a spontaneous instability of plane flame propagation of Taylor-Markstein type (Strelow, 1984) or Darrieus-Landau type (Dunn-Rankin et al, 1986). In this respect, we mention that Fernandez and Guillard (1989.b) have computed the development of a tulip flame instability from an

initially planar flame. This experiment has been reconducted in the present work leading once again to the formation of a tulip flame (we do not display here the results of this simulation as they are similar to the ones presented by Fernandez and Guillard (1989.b). This seems to indicate that a spontaneous instability mechanism is present in the tulip formation.
Before concluding, it is worth noticing two numerical facts indicating the sensibility of the tulip phenomena to perturbations. The first one concerns the linear solver used in the implicit part of the algorithm. As explained in Section 2, we use a symmetric Gauss-Seidel algorithm to solve the linear system arising from the implicit temporal discretisation. We have observed in our experiments that the flame becomes asymmetric if we do not solve this linear system with high enough accuracy at each time step; this indicates that this flame is very sensible to small perturbations. The second fact is related to the accuracy of the numerical approximation. If, instead of using a second-order accurate approximation of the hyperbolic fluxes, we use a first-order accurate approximation, then the tulip formation is not observed, although the computed values of the gas velocity are of the same order in the two cases; again, this confirms the important influence of pertubations on the development of the tulip flame.

6. Conclusion

The present work has numerically investigated the development of the tulip instability in a rectangular adiabatic closed box and the results have been compared with the experiments by Steinert et al. (1982), Dunn-Rankin (1985) and Dunn-Rankin et al. (1986). Despite the shortcomings of the numerical method (in particular, the rather low activation energy used in order to reduce the computational costs) the agreement with the experimental data is very satisfactory. Comparisons of the average flame shapes digitized from Schlieren photographs (Steinert et al, 1982) and our computed reaction rate contours show that the calculations are able to reproduce the temporal development of the flame with a good accuracy. Concerning the velocity field generated by the flame, the main difference between the LDA measurements by Dunn-Rankin (1985) and the present results is the presence of negative velocities in the burnt gases while the experiments show the persistence of positive velocity almost until the emergence of the tulip flame. Note however that the results by Gonzalez et al. (to be published) also show negative velocities in the burnt gases after the interaction of the flame with the side walls.

The present results do not give a definite answer about the cause of the tulip flame phenomenon, but they seem to favour the interpretation of this phenomenon as a manifestation of a Darrieus-Landau type instability. We hope to have shown that the development of appropriate numerical methods make them now an accurate and useful tool for this type of studies.

ACKNOWLEDGEMENT

We thank Prof R.F. SAWYER for kindly allowing us to reproduce the figure of his work with W. STEINERT and D. DUNN-RANKIN.

Reaction rate contours corresponding to $t_{12} = 31.62ms$ (Duct dimensions: $L_x = 150\,mm$, $L_y = 38.1\,mm$).

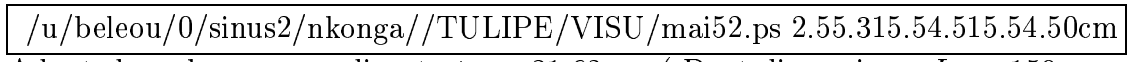

Adapted mesh corresponding to $t_{12} = 31.62\,ms$ (Duct dimensions: $L_x = 150\,mm$, $L_y = 38.1\,mm$).

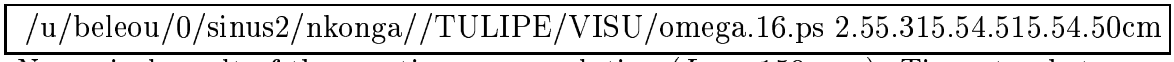

Numerical result of the reaction zone evolution ($L_x = 150\,mm$): Time step between flame shape contours is $\simeq 1.85\,ms$ from $t_1 = 3.72\,ms$ to $t_8 = 16.74\,ms$, then $3.70\,ms$ to $t_{12} = 31.62ms$ and from $t_{13} = 44.65\,ms$ to the end.

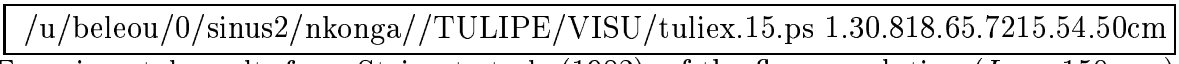

Experimental result, from Steinert et al. (1982), of the flame evolution ($L_x = 150mm$): Digitized flame shapes obtained from Schlieren movies; time step is $1.85\,ms$ to (*) then $3.70\,ms$. This figure is courtesy of Prof. R.F. Sawyer

Figure 2. Experimental and numerical pressure evolution ($L_x = 150mm$): The experimental curve from Steinert et al. (1982) is courtesy of Prof. R.F. Sawyer

/u/beleou/0/sinus2/nkonga//TULIPE/VISU/omega.8.ps 2.55.33.54.57.09.0cm

Numerical result of the reaction zone evolution ($L_x = 30\,mm$): time step between flame shape contours is approximately $1.85\,ms$

/u/beleou/0/sinus2/nkonga//TULIPE/VISU/tuliex.3.ps 1.750.91013.67.09.0cm

Experimental result of the flame evolution ($L_x = 30\,mm$): Digitized flame shapes obtained from schlieren movies; time step is $1.85\,ms$. This figure is courtesy of Prof. R.F. Sawyer

/u/beleou/0/sinus2/nkonga//TULIPE/VISU/omega.20.ps 2.55.312.4.515.55.81cm

Numerical result of the reaction zone evolution ($L_x = 120\,mm$): time step between flame shape contours is approximately $1.85\,ms$ to $t_8 = 16.74\,ms$ then $3.70\,ms$

/u/beleou/0/sinus2/nkonga//TULIPE/VISU/tuliex.12.ps 2.33.015.6.0015.55.81cm

Experimental result of the flame evolution ($L_x = 120\,mm$): Digitized flame shapes obtained from schlieren movies; time step is $1.85ms$ to (*) then $3.70ms$. This figure is courtesy of Prof. R.F. Sawyer

$t = 9.30\,ms$

/u/beleou/0/sinus2/nkonga//TULIPE/VISU/fig7.ps 2.58.612.010.015.012.5cm

Figure 3. Velocity field near the flame front at $t = 9.30\,ms$ ($L_x = 150mm$). The reaction rate contours corresponding to one half of the maximum value of the reaction rate are superposed upon the velocity field. To make the figure clearer, only one mesh point over three in the y-direction and one three two in the x-direction are plotted.

$t = 13.04\,ms$

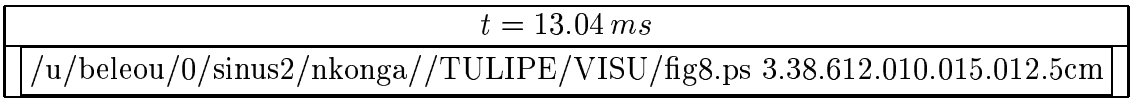

Figure 4. Velocity field near the flame front at $t = 13.04\,ms$ ($L_x = 150mm$). The reaction rate contours corresponding to one half of the maximum value of the reaction rate are superposed upon the velocity field. To make the figure clearer, only one mesh point over three in the y-direction and one three two in the x-direction are plotted.

Figure 5. Horizontal velocity profiles on the wall between $t_7 = 14.88\,ms$ and $t_{12} = 31.62\,ms$ ($L_x = 150mm$). Time step is approximately $1.85\,ms$ from $t_8 = 16.74\,ms$ to t_{12}. The tulipe instability begins between $t_{10} = 24.19\,ms$ and $t_{11} = 27.91\,ms$.

$t = 24.19\,ms$

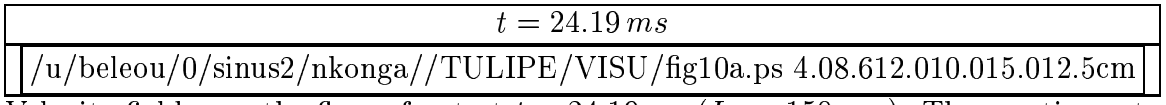

Velocity field near the flame front at $t = 24.19\,ms$ ($L_x = 150mm$). The reaction rate contours corresponding to one half of the maximum value of the reaction rate are superposed upon the velocity field. To make the figure clearer, only one mesh point over three in the y-direction and one three two in the x-direction are plotted.

$t = 27.91\,ms$

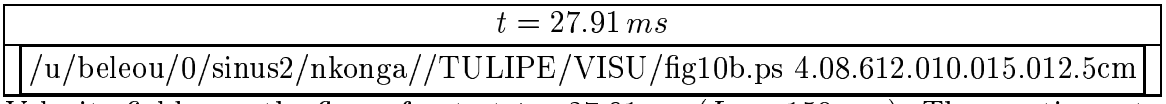

Velocity field near the flame front at $t = 27.91\,ms$ ($L_x = 150mm$). The reaction rate contours corresponding to one half of the maximum value of the reaction rate are superposed upon the velocity field. To make the figure clearer, only one mesh point over three in the y-direction and one three two in the x-direction are plotted.

$t = 31.63\,ms$

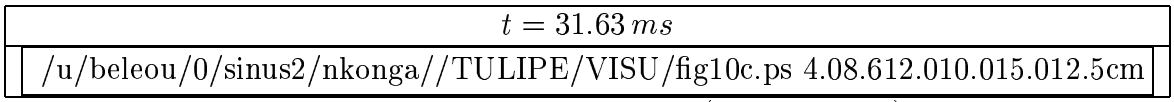

Velocity field near the flame front at $t = 31.63\,ms$ ($L_x = 150mm$). The reaction rate contours corresponding to one half of the maximum value of the reaction rate are superposed upon the velocity field. To make the figure clearer, only one mesh point over three in the y-direction and one three two in the x-direction are plotted.

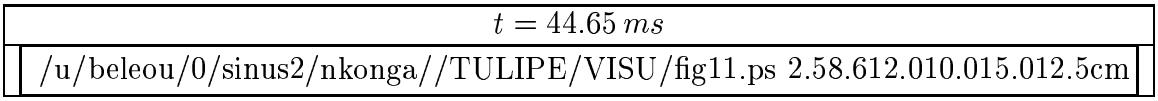

Figure 6. Velocity field near the flame front at $t = 44.65\,ms$ ($L_x = 150mm$). The reaction rate contours corresponding to one half of the maximum value of the reaction rate are superposed upon the velocity field. To make the figure clearer, only one mesh point over three in the y-direction and one three two in the x-direction are plotted.